ACS NANO

www.acsnano.org

ARTICLE

Toward Phonon-Limited Transport in Two-Dimensional Transition Metal Dichalcogenides by Oxygen-Free Fabrication

Subhrajit Mukherjee, Shuhua Wang, Dasari Venkatakrishnarao, Yaoju Tarn, Teymour Talha-Dean, Rainer Lee, Ivan A. Verzhbitskiy, Ding Huang, Abhishek Mishra, John Wellington John, Sarthak Das, Fabio Bussolotti, Thathsara Deshani Maddumapatabandi, Yee Wen Teh, Yee Sin Ang,* Kuan Eng Johnson Goh,* and Chit Siong Lau*

Cite This: *ACS Nano* 2025, 19, 9327−9339

Read Online

ACCESS | Metrics & More | Article Recommendations | Supporting Information

ABSTRACT: Developing future electronics will require aggressive scaling of the channel material thickness while maintaining device performance. Two-dimensional (2D) semiconductors are promising candidates to sustain further device scaling, but despite more than two decades of intense research, experimental performance continues to lag theoretical expectations. Here, we develop an oxygen-free approach to fabricate 2D field-effect transistors and push the electrical transport toward the theoretical phonon-limited intrinsic mobility. This approach achieves record carrier mobilities of 91 and 132 $cm^2 V^{-1} s^{-1}$ for mono- and bilayer MoS_2 transistors on silicon oxide substrates. Statistical analysis of over 60 MoS_2 and WS_2 devices confirms that oxygen-free fabrication enhances device performance by more than an order of magnitude across key figures of merit. While previous studies suggest that 2D transition metal dichalcogenides such as MoS_2 and WS_2 are relatively stable in air, we show that even short-term ambient exposure can degrade their performance. We identify oxygen as a crucial factor in limiting transistor performance through irreversible chemisorption. This study emphasizes the criticality of avoiding oxygen exposure and offers guidance for device manufacturing that impacts fundamental research and practical applications of 2D materials.

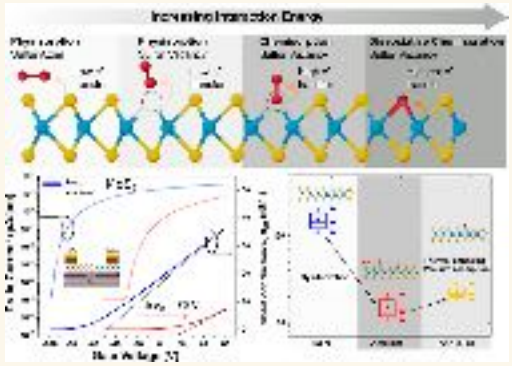

KEYWORDS: *2D materials, 2D semiconductors, carrier mobility, field-effect transistor, MoS_2, WS_2*

INTRODUCTION

Silicon complementary metal-oxide-semiconductor (CMOS) technology has been pivotal in the progress of modern electronics. Advances in nanofabrication techniques have enabled continued scaling of CMOS transistor technology.[1] Meeting the growing demand for cheaper, faster, and more energy-efficient electronics will require the ultimate scaling of the semiconductor channel thickness toward the sub-nanometre regime. However, achieving this with any three-dimensional semiconductor is challenging due to the increased surface roughness scattering from dangling bonds that severely degrades carrier mobility.[2] 2D transition metal dichalcogenide (TMD) semiconductors with intrinsic atomic-scale thickness (<1 nm) could be a solution.[3−9] Their van der Waals (vdW) layered nature provides dangling-bond-free surfaces such that high carrier mobilities are maintained even in monolayer devices. This has positioned 2D TMDs on the technology roadmap of industry, including companies such as the Taiwan Semiconductor Manufacturing Corporation (TSMC), Samsung, Intel, and IMEC.[10] However, despite promising early device prototypes, 2D TMD transistor performance falls short of their theoretical expectations.[11−13] Realizing their full potential will depend on developing high-quality material growth, controlled doping, dielectric integration, and contact engineering methods.[4,7,9,10] Encouragingly, there has been considerable progress in these areas. Chemical vapor deposition can produce highly crystalline materials with fewer defects and impurities to rival exfoliated material

Received: January 16, 2025
Revised: February 7, 2025
Accepted: February 10, 2025
Published: February 24, 2025

https://doi.org/10.1021/acsnano.5c00995
ACS Nano 2025, 19, 9327−9339

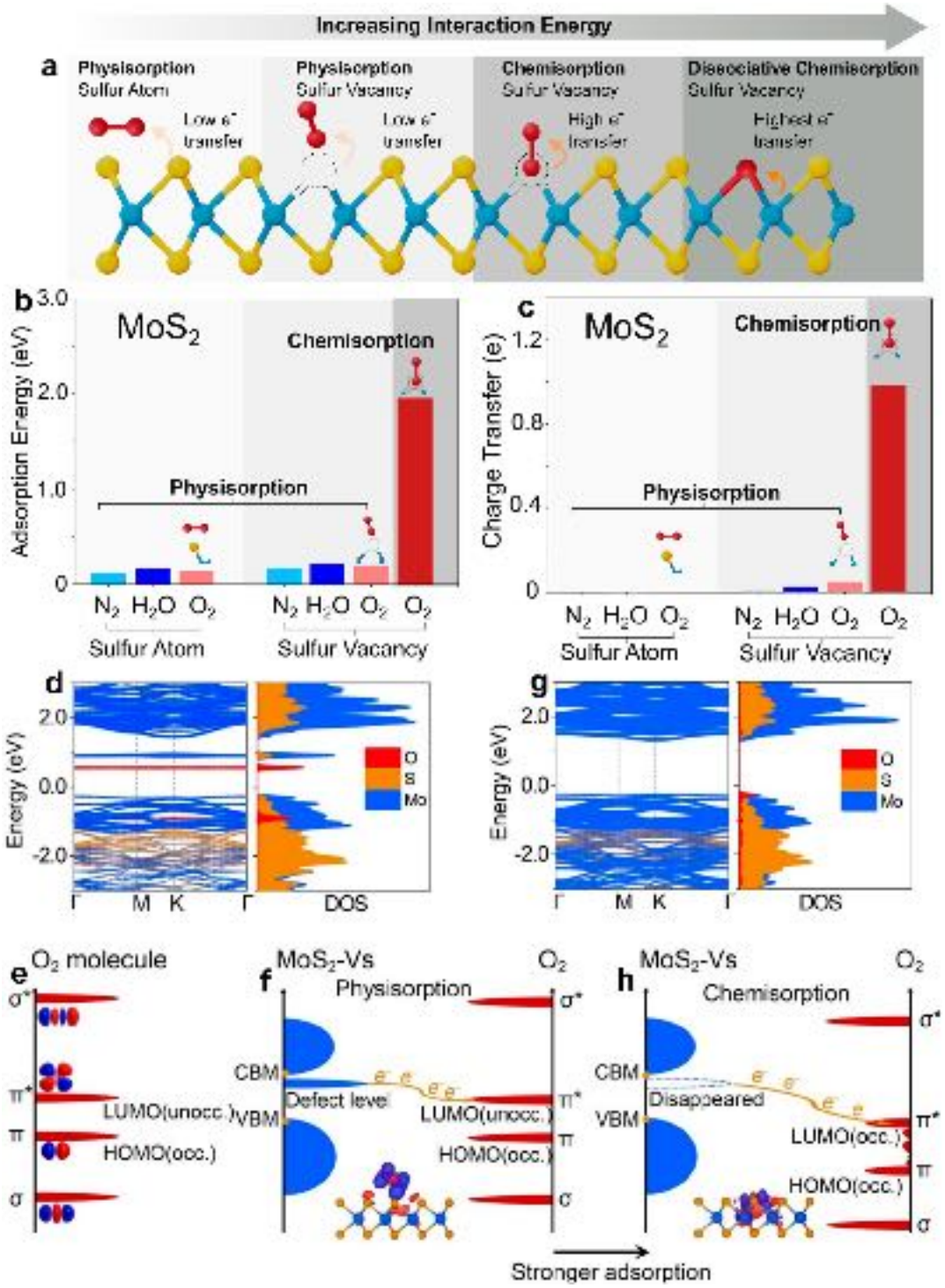

Figure 1. Molecular adsorption on monolayer TMDs. (a) Schematic of possible diatomic molecular adsorbate interaction scenarios with a monolayer TMD. The dotted outlines represent a sulfur vacancy V_S. (b) Adsorption energy of O_2, N_2, and H_2O on the pristine surface and sulfur vacancy sites of a monolayer MoS_2, and resultant (c) electron transfer from TMDs to molecular adsorbates. Electronic band structure and the projected density of states (PDOS) of MoS_2 with sulfur vacancies V_S during O_2 (d) physisorption and (g) chemisorption. (e) Molecular orbital diagram of the O_2 molecule showing the highest occupied molecular orbital (HOMO) and lowest unoccupied molecular orbital (LUMO). Schematic of the electron transfer process and local electronic structure during O_2 physisorption (f) and chemisorption (h) on defective MoS_2. The embedded plot shows the charge density difference, where blue regions represent electron accumulation and red regions represent electron depletion. Electrons transfer from TMD to the LUMO of O_2 and accumulate on the O_2 molecule in the shape of π orbitals.

quality.[14−16] The vdW interfaces formed between TMDs and three-dimensional (3D) metals e.g. In,[17,18] Bi[19], Pt,[20] and Sb,[21,22] as well as Y-doping[23] of source-drain contact regions, have led to ultralow contact resistances. Surface,[24] substitutional,[25] and substoichiometric oxide[26,27] doping have increased sheet conductance and on-state currents. Dielectric

https://doi.org/10.1021/acsnano.5c00995
ACS Nano 2025, 19, 9327−9339

and substrate engineering can effectively quench impurity and phonon scattering to enhance carrier mobilities.[28−32] These advances have narrowed the experiment-theory device performance gap and showed that progress depends on tailored solutions that consider the unique nature of 2D materials; their extreme geometry.

2D geometry with extreme surface-to-volume ratio heightens the sensitivity of 2D materials to their environment.[33−37] A monolayer TMD comprises a three-atom crystal lattice where the layer of transition metal atoms is sandwiched between two layers of chalcogens. The chalcogen atoms form a surface that can interact with ambient molecular absorbates. There are four possible interaction scenarios for molecular adsorbates on TMD surfaces (illustrated in Figure 1a).[34] These are broadly categorized into weakly interacting physisorption and strongly interacting chemisorption. Physisorption of a molecular adsorbate occurs on a (i) sulfur atom or (ii) sulfur vacancy (V_S), while chemisorption may exhibit either (iii) non-dissociative or (iv) dissociative coupling to a V_S. For dissociative chemisorption, the absorbate molecule dissociates into individual atoms which substitutionally replaces a V_S site. This substitution causes a disruptive and often permanent stoichiometry change, e.g., chemical oxidation. Ambient oxidation is an undesired material degradation of TMDs. It is well documented, as changes in stoichiometry are easily detected by experimental techniques like X-ray photoemission spectroscopy (XPS) (see Supporting Information Figure S1) or Raman and photoluminescence spectroscopy.[37−42] In contrast, physisorption (i, ii) is often considered a reversible process where its smaller interaction energies allow adsorbate removal through thermal annealing or vacuum cycling.[43,44] Consequently, TMDs such as MoS_2 and WS_2 are often considered ambient stable as many studies have confirmed their short-term resistance against (iv) dissociative chemical oxidation. However, the impact and reversibility of non-dissociative (iii) chemisorption remain elusive. Although some theoretical studies[34] have hinted at its significance, this process remains poorly understood due to challenges in experimental validation, especially at the device level, where ambient exposure is unavoidable in standard cleanroom fabrication.

In this work, we study the impact of ambient molecular exposure on the performance of 2D TMD transistors. Using a purpose-built facility, we can complete the entire fabrication of 2D devices in an inert argon environment. We found that minimizing oxygen exposure throughout the fabrication process results in more than an order of magnitude enhancement across key transistor figures of merit, such as carrier mobility, sheet conductance, and carrier density. This enables us to push our device carrier mobility toward the theoretical limit arising from intrinsic phonon scattering.[11−13,45] Recognizing molecular oxygen as a critical factor limiting device performance sets a significant milestone. This marks a qualitative step in bridging the theoretical-experimental discrepancy and guides the manufacture of high-performance 2D devices for fundamental research and practical applications.

RESULTS

To understand the impact and likelihood of physisorption and non-dissociative chemisorption (hereafter referred to as chemisorption in the rest of the manuscript for simplicity), we first perform adsorption energy (E_{ad}) and charge transfer (Δq) analysis using density functional theory (DFT) simulations (details in Methods, and Supporting Information Note-1 and Figures S2−S11). The simulations evaluate the interactions of common ambient molecules O_2, N_2, and H_2O with monolayer MoS_2 and WS_2. Using a $4 \times 4 \times 1$ supercell, we consider both pristine (no V_S) and defective (single V_S) monolayers. Such a supercell size corresponds to a defect density of $\sim 7.1 \times 10^{13}$ cm^{-2}, comparable to expected experimental values.[46] We calculate the E_{ad} of O_2, N_2, and H_2O for MoS_2 (Figure 1b) and WS_2 (Supporting Information Figure S10a). In pristine TMDs, all studied molecules show weak physisorption with characteristic energies $E_{ad} \sim 114-176$ meV. In contrast, sulfur vacancies in TMDs promote the chemisorption of O_2 to the V_S site, while interactions with N_2 and H_2O remain limited to physisorption (Supporting Information Table-T1). Notably, O_2 chemisorption is significantly stronger than physisorption, with E_{ad} values almost an order of magnitude larger, $E_{ad} \sim 1.95-2.34$ eV. Consequently, this strong interaction between O_2 and V_S, coupled with the large electronegativity of molecular oxygen, should result in substantial charge transfer at the chemisorption site. Indeed, our Bader charge analysis confirms this behavior (Figure 1c and Supporting Information Figure S10b). O_2 chemisorption leads to considerably more charge transfer with $\Delta q = 0.91$ e for MoS_2 (Figure 1c) and 1.08 e for WS_2 (Supporting Information Figure S10b) compared to physisorption, where $\Delta q < 0.049$ e for O_2, N_2, and H_2O (Supporting Information Table-T1). As further validation, calculations performed using different-sized supercells and defect densities show similar trends for E_{ad} and Δq (Supporting Information Figure S11 and Table-T2). The calculated band structure shows that V_S on the surface of TMDs act as electron donors and induce localized defect states in the band gap. When O_2 molecules are physisorbed at the V_S site, the lowest unoccupied molecular orbitals (LUMO) of O_2 are slightly below the defect levels, suggesting potential electron transfer from the TMD to the O_2 molecules (Figure 1d−f). In contrast, the chemisorption of O_2 fills the V_S sites with oxygen atoms, leading to the disappearance of the defect level. Electron transfer results in the complete occupation and delocalization of the O_2 LUMO (Figure 1g,h). These simulation results suggest that O_2 exposure can affect TMD device performance. Even for ambient stable TMDs with low defect densities, the large E_{ad} of O_2 chemisorption can lead to unwanted and irreversible *p*-doping. Uncontrolled doping from ambient molecular adsorbates at the source/drain and channel regions leads to detrimental effects such as larger parasitic contact resistance, undesired shift in threshold voltage, and lowered sheet conductance. As our experiments were conducted inside argon-filled gloveboxes, we also evaluated the impact of Ar adsorption (Table T3 and Figure S12 in Supporting Information). The calculations reveal no tendency for chemical bond formation or significant charge transfer between Ar and the TMD layers in either the pristine or defective states. Electronic band structure analysis shows that the weak Ar physisorption does not alter the electronic properties of the monolayers, confirming the chemical inertness of Ar toward TMD surfaces.

However, experimentally assessing the impact on devices from strongly chemisorbed O_2 is challenging. So far, studies have measured the effects on 2D TMD devices from weakly physisorbed molecules and shown that it is reversible through vacuum and thermal cycling.[43,44] Evaluating the impact from potentially irreversible chemisorbed molecules will require

https://doi.org/10.1021/acsnano.5c00995
ACS Nano 2025, 19, 9327−9339

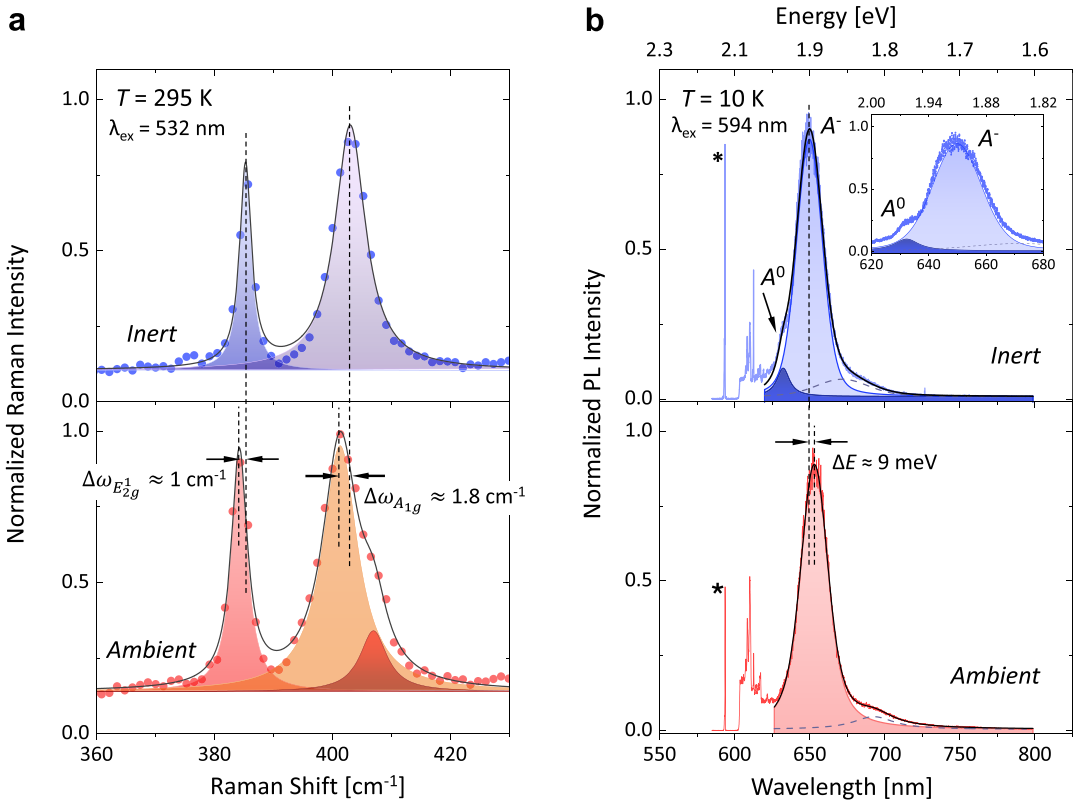

Figure 2. Optical spectroscopy. (a) Raman spectra of a monolayer MoS_2 prepared in (top-panel) inert and (bottom-panel) ambient environments, recorded at room temperature under 532 nm laser excitation. Experimental data points (solid circles) are fitted (black lines are summed peaks), using Lorentzian peak-fit, where the different color-shaded regions show individual phonon modes. The ambient MoS_2 monolayer exhibits significant broadening and downshift to lower wave numbers (i.e., softening) of the A_{1g} mode attributed to the oxygen adsorption-driven charge doping. Moreover, the distinct A_{1g} mode splitting (401.3 and 406.9 cm^{-1}) corresponding to electron transfer further supports our O_2-induced doping hypothesis, whereas the left E^1_{2g} mode is virtually unchanged. (b) Photoluminescence spectra recorded at 10 K under 594 nm CW laser excitation for the same monolayers of MoS_2 prepared in (top) inert, and (bottom) ambient conditions. The inert monolayer shows both neutral exciton (A^0) and trion (A^-) signatures, while molecular O_2 adsorption suppresses excitonic features due to enhanced trion formation from charge doping. The inset shows a close up of the exciton and trion peaks. The trion peak redshift (~9 meV) reflects a Fermi level E_F shift from doping in the system, consistent with electrical measurements (Figure 3). Detailed measurements, mapping and optical images of the monolayers are provided in the Supporting Information for both Raman (Figures S14 and S15) and PL measurements (Figure S17). The asterisk (*) denotes the laser line and high energy features beyond the exciton originating from the different Raman lines from the sample.

minimal ambient exposure, even during material synthesis and device fabrication. Currently, 2D TMDs are commonly synthesized through mechanical exfoliation or chemical vapor deposition (CVD). Exfoliation is usually conducted in standard laboratory or cleanroom environments. It can also be performed relatively quickly in controlled environments, such as an inert argon-filled glovebox with minimal O_2 and H_2O levels. However, for CVD-grown TMDs, limiting ambient exposure is difficult due to the technical challenge of integrating large-growth furnace tubes with gloveboxes. More significant concerns are the materials processing and device fabrication steps. CVD films are typically wet transferred from growth to device substrates. Also, device fabrication will require cleanroom lithography and thin film deposition processes, which must now be in controlled inert conditions.

We first assess the impact of ambient exposure in 2D TMDs via Raman spectroscopy. A substantial charge transfer doping in monolayer MoS_2 primarily affects the out-of-plane (A_{1g}) phonon mode leading to peak position shifts and splitting with increased full width at half maximum (FWHM).[47,48] We performed room-temperature micro-Raman spectroscopy (μRS) for inert (top panel) and ambient (bottom panel) exfoliated monolayer MoS_2 (Figure 2a). In the inert sample, we measure typical in-plane ($E_{2g}{}^1$) and out-of-plane (A_{1g}) Raman modes at ~385 and ~403 cm^{-1}, respectively, with a peak separation of ~18 cm^{-1}. This peak separation is consistent with reported values for monolayer MoS_2.[49] In contrast, charge transfer doping in ambient samples results in downshifted Raman signatures, and a significant broadening and peak splitting of the A_{1g} mode compared to the inert sample (Figure 2a). Full Raman maps for both $E_{2g}{}^1$ and A_{1g} modes and the peak separation and FWHM are also shown in Figure S14–S15 of the Supporting Information. We measure an increase in the A_{1g} mode's FWHM from 8 to 12 cm^{-1}. This broadening corresponds to an estimated charge doping density of ~4 × 10^{12} cm^{-2}.[50] This is corroborated by the estimated charge doping of ~(3–4) × 10^{12} cm^{-2} based on the shift of ~1.8 cm^{-1} for the A_{1g} peak (calculation details are available in Supporting Information).

Likewise, significant charge transfer doping should also be reflected in low-temperature photoluminescence spectroscopy (PL) through peak shifts of excitonic species. For the inert MoS_2 monolayer, the PL spectrum (top-panel in Figure 2b) displays two clear peaks: the optically bright neutral exciton

https://doi.org/10.1021/acsnano.5c00995
ACS Nano 2025, 19, 9327–9339

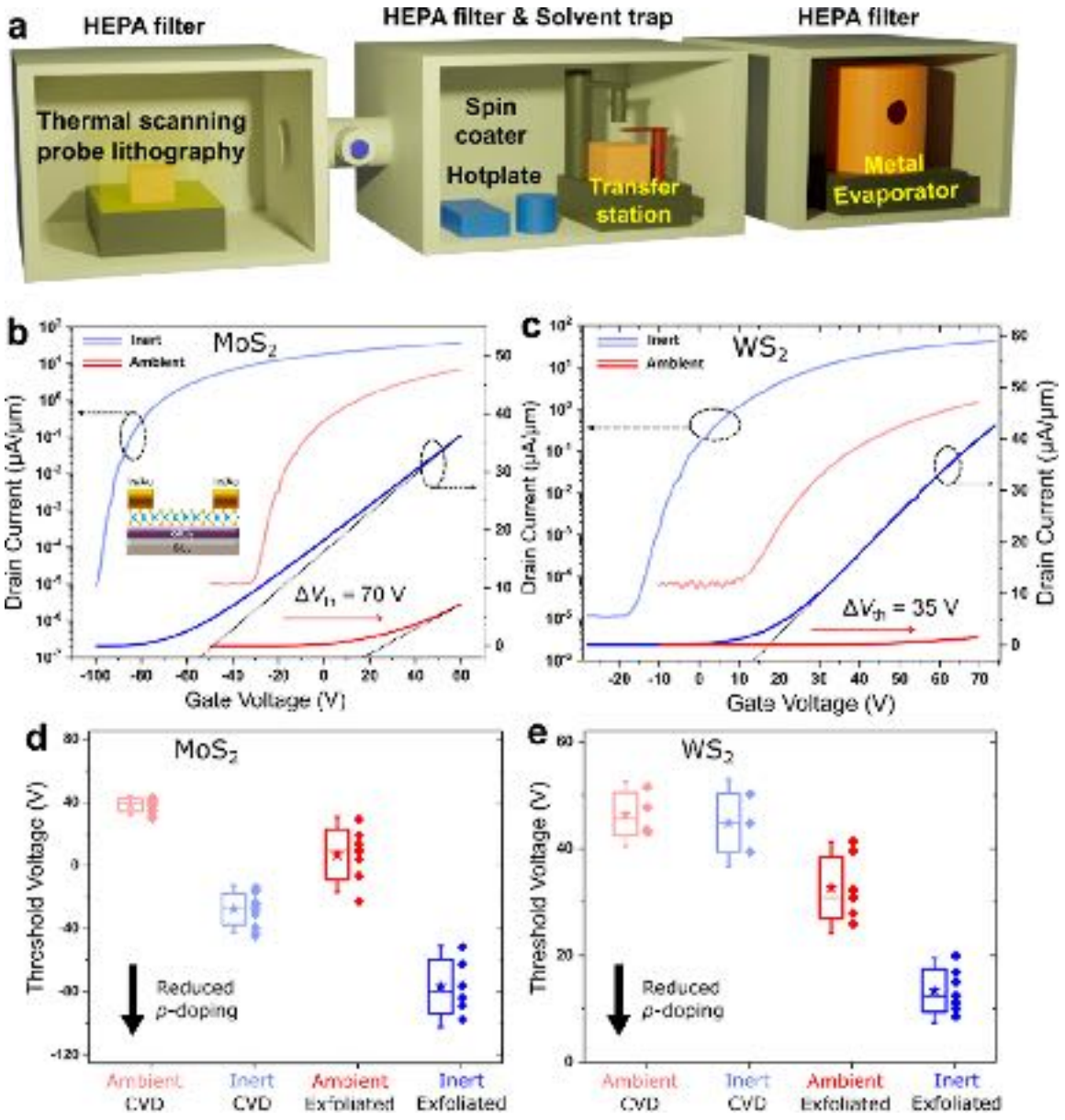

Figure 3. Charge doping from oxygen. (a) Schematic of our purpose-built fabrication facility, which allows complete fabrication of 2D devices in an argon environment with typical O_2 and H_2O levels maintained below 5 ppm, usually <1 ppm. Capabilities include 2D material transfer, wet chemistry, thermal scanning probe nanolithography, and metal deposition. Transfer characteristics of a monolayer (b) MoS_2 and (c) WS_2 back-gate field-effect transistor at a drain voltage V_D = 1 V. The device schematic is shown as an inset. The device channel lengths are 1 μm. The dotted lines represent the linear extrapolation to obtain threshold voltages (V_{th}). Boxplots present statistical distributions of the extracted threshold voltages for (d) MoS_2 and (e) WS_2 devices. Significant negative shifts in threshold voltages are observed for inert devices compared to their ambient counterpart, which indicate reduced O_2-driven p-doping.

transition (A^0) appears at 633 nm, and the trion resonance (A^-) at 650 nm as expected for monolayers. In contrast, the ambient-exposed MoS_2 monolayer exhibits trion dominated PL emission, accompanied by a shift in the trion peak position and strong suppression of exciton oscillator strength. The neutral exciton peak quenching is likely due to charge screening of Coulomb interactions, while the trion peak shift (~9 meV) is attributed to charge transfer doping from adsorbed oxygen molecules to the TMD monolayer.[51] We can estimate the carrier concentration in TMD monolayers from the exciton-trion splitting ($\Delta E_{XT} = A^- - A^0$), as the ΔE_{XT} is strongly influenced by the Fermi energy.[52] Our measured trion peak shift of ~9 meV corresponds to an estimated doping density of ~2×10^{12} cm^{-2}, consistent with our Raman analysis (calculation details can be found in the Supporting Information). This estimated doping level agrees well with previous studies on doped 2D TMDs.[53]

Next, to experimentally evaluate the impact of molecular chemisorption on TMD devices, we designed a solution for TMD device fabrication with minimal ambient exposure.[54] Our approach is based on purpose-built gloveboxes integrated with nanolithography, thin film deposition, and solvent processing capabilities (Figure 3a and Supporting Information Figure S13), with typical O_2 and H_2O levels maintained below 5 ppm. To ensure consistency, all devices were fabricated and measured using the same experimental tools, except that inert

https://doi.org/10.1021/acsnano.5c00995
ACS Nano 2025, 19, 9327−9339

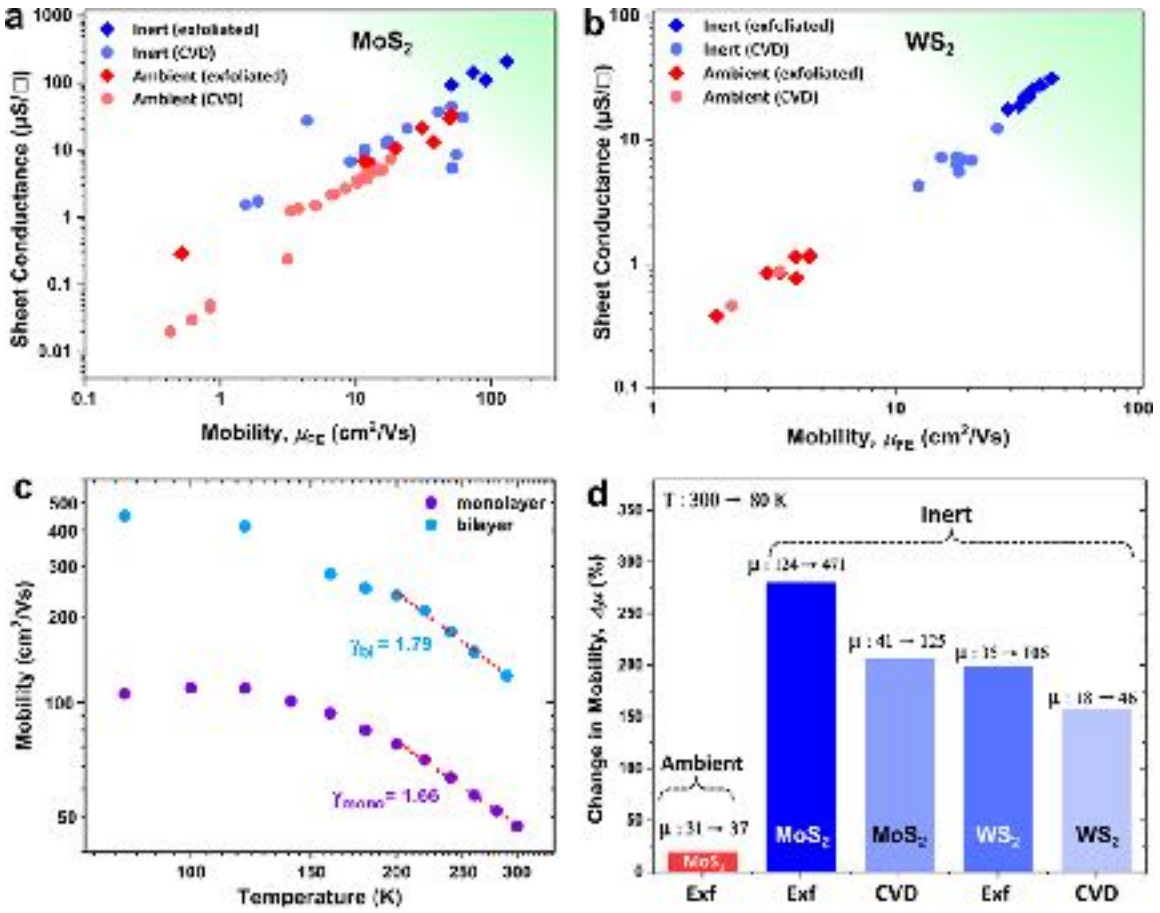

Figure 4. Electrical data of inert MoS_2 FETs. Distribution of field-effect mobility (μ_{FE}) vs sheet conductance (σ_{2D}) for (a) MoS_2 and (b) WS_2 field-effect transistors (FETs) fabricated in inert (blue) and ambient (red) conditions. Mean mobility values show up to ~2 orders of magnitude increase for inert devices compared to ambient devices. Similarly, sheet conductance is enhanced by up to ~3 orders for MoS_2 and ~2 orders for WS_2. (c) Temperature dependent mobility characteristics of a monolayer and bilayer transistor, showing mobility improvement with decreasing temperature. Mobility μ quenching at higher temperatures is due to phonon scattering ($\mu \propto T^{-\gamma}$). (d) When the temperature is decreased from 300 to 80 K, significant enhancement is observed for inert devices compared to ambient devices, showing higher impurity-limited mobility for inert devices.

devices were fabricated entirely inside the glovebox. In contrast, ambient devices were exposed to air during exfoliation, development, and liftoff. Measurement conditions were also kept similar. Specific details are mentioned in the Methods section. For this study, we fabricated sets of MoS_2 and WS_2 back-gated FETs on 290 nm SiO_2/Si^{++}, utilizing both exfoliated and CVD materials. All devices fabricated in our glovebox facility are hereafter referred to as "inert." We fabricated equivalent device sets in ambient conditions as a control, hereafter referred to as "ambient." In total, 38 MoS_2 and 24 WS_2 devices were measured for statistical analysis of FET metrics, including threshold voltage, sheet conductance, mobility, hysteresis, and interfacial trap densities.

Our theoretical results suggest that O_2 chemisorption leads to substantial charge transfer doping. We can determine the degree of charge doping by comparing the threshold voltages V_{th} of ambient and inert devices. Room temperature transfer curves of representative exfoliated monolayer MoS_2 and WS_2 inert (blue) and ambient (red) devices are shown in Figure 3b,c, where we observe typical *n*-type semiconducting behavior. Consistent with our theoretical expectations, ambient devices exhibit substantial *p*-doping due to electron transfer from TMDs to the molecular adsorbates. This *p*-doping is characterized by significant shifts in V_{th} toward positive gate voltages with ΔV_{th} = 70 V (MoS_2) and 35 V (WS_2) corresponding to an electron doping of ~5.1×10^{12} cm^{-2} (MoS_2) and ~3.3×10^{12} cm^{-2} (WS_2). Figure 3d (MoS_2) and 3e (WS_2) show statistics summarizing V_{th} distributions. We observe significant doping for MoS_2 where mean ΔV_{th} = 90 V (exfoliated) and 65 V (CVD) corresponding to an electron *n*-doping of ~6.5×10^{12} cm^{-2} (exfoliated) and ~4.7×10^{12} cm^{-2} (CVD). For WS_2, we find more modest doping with mean ΔV_{th} = 19 V (exfoliated) and 3 V (CVD) corresponding to an electron doping of ~1.3×10^{12} cm^{-2} (exfoliated) and ~2.2×10^{11} cm^{-2} (CVD). These values are consistent with the doping estimated from our optical studies in Figure 2.

The observed difference in doping levels between MoS_2 and WS_2 is surprising. Our DFT calculations suggest negligible differences in Δq, and defect densities are also expected to be lower in MoS_2 crystals with better growth quality, which should present fewer V_S sites for O_2 chemisorption. A possible explanation is that more defective WS_2 crystals tend to undergo dissociative oxidation from defect pairing.[34,40] The kinetics for dissociative oxidation likely differ from chemisorption and may be material-dependent. Furthermore, differences in overall stoichiometry, purity, and crystallinity are expected between MoS_2 and WS_2 crystals, suggesting more complex O_2 interaction mechanisms. However, the difference

https://doi.org/10.1021/acsnano.5c00995
ACS Nano 2025, 19, 9327−9339

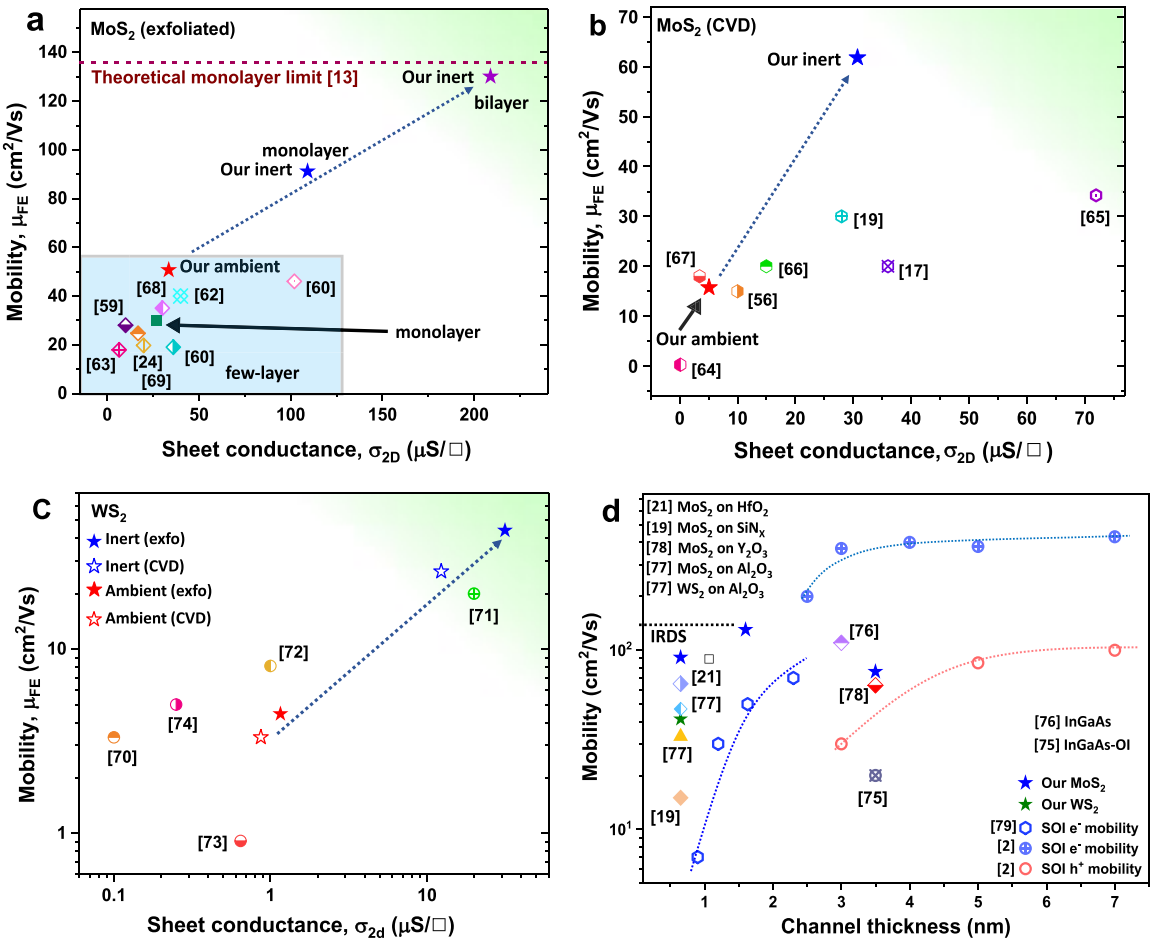

Figure 5. Benchmarking FET performance against the existing literature for (a) exfoliated MoS_2 and (b) CVD MoS_2. The red dashed line represents the theoretical monolayer limit of the room-temperature, phonon-limited mobility in 2D MoS_2. We benchmark the sheet conductance and back-gated field-effect mobility of FETs with comparable geometries on SiO_2.[17,19,24,56,59−69] (c) Benchmarking FET performance against the existing literature for exfoliated and CVD WS_2. Solid (hollow) stars represent exfoliated (CVD) FETs.[70−74] (d) We also benchmark mobility as a function of FET channel thickness. We compare our devices with other state-of-the-art 2D FETs, traditional ultrathin body (UTB) silicon PMOS and NMOS, III−V 2DEG MOSFETs, and IRDS roadmap targets.[2,19,21,75−79]

in doping levels observed between CVD and exfoliated materials is expected. Exfoliated devices represent the lowest defect density and ambient exposure levels where 2D flakes are prepared inside the gloveboxes. For commercially purchased CVD TMDs, the postgrowth packaging and shipment process is beyond our control. CVD devices thus represent higher defect densities and a "medium" ambient exposure level, translating to more significant *p*-doping.

Minimizing ambient exposure to prevent unwanted *p*-doping enables our devices to reach high carrier densities up to ~1.2×10^{13} cm^{-2} (MoS_2) and ~5.2×10^{12} cm^{-2} (WS_2). For context, our MoS_2 carrier densities approach degenerate doping levels[55] and are comparable with intentional surface charge transfer or solid-state doping techniques (~$1-2 \times 10^{13}$ cm^{-2}).[24,26,55] As a result, inert devices can attain more than an order of magnitude larger on-state current I_{ON} and current on/off ratios than their ambient counterparts (Figure 3b,c). Our inert monolayer MoS_2 FET reached I_{ON} ~280 $\mu A/\mu m$ (Supporting Information Figure S18), exceeding even ultrashort channel (~29 nm) FETs developed by IMEC (250 $\mu A/\mu m$).[56] Current on/off ratios for inert devices (>10^6) exceed ambient devices (~10^4-10^5) by around an order of magnitude. Such significant *n*-doping was previously only achieved by intentional doping techniques. However, these techniques can introduce foreign impurities that lead to impurity-related Coulomb scattering or band structure changes impacting electrical transport, lowering carrier mobilities and sheet conductance. For example, our DFT calculations also suggest that the chemisorption of O_2 molecules can lead to band structure changes that increase effective mass and lower carrier mobility (Supporting Information Figure S19 and Table-T4). In contrast, such effects are not expected for our approach, which minimizes ambient adsorbates to preserve the intrinsic cleanliness of 2D TMDs.

To investigate whether minimizing ambient adsorbates translates into superior electrical transport, we extract the carrier mobility and sheet conductance from room-temperature transport measurements of 38 MoS_2 (Figure 4a) and 24 WS_2 (Figure 4b) few-layer and monolayer devices (details in Methods). Clear improvements are observed for inert (blue) compared to ambient (red) devices made from both exfoliated (diamond markers) and CVD (circle markers) materials. For exfoliated (CVD) MoS_2, we find that the mean mobility increases by a factor of ~3 (3) to 86.5 ± 16.7 $cm^2/(V\,s)$ (25.7 ± 5.8 $cm^2/(V\,s)$), while the mean sheet conductance increases by a factor of ~9 (6) to 138.8 ± 25.5 $\mu S/\square$ (16.5 ± 3.6 $\mu S/\square$). Similar improvements are observed for exfoliated (CVD) WS_2, with mean mobility increasing by a factor of ~10 (26) to

https://doi.org/10.1021/acsnano.5c00995
ACS Nano 2025, 19, 9327−9339

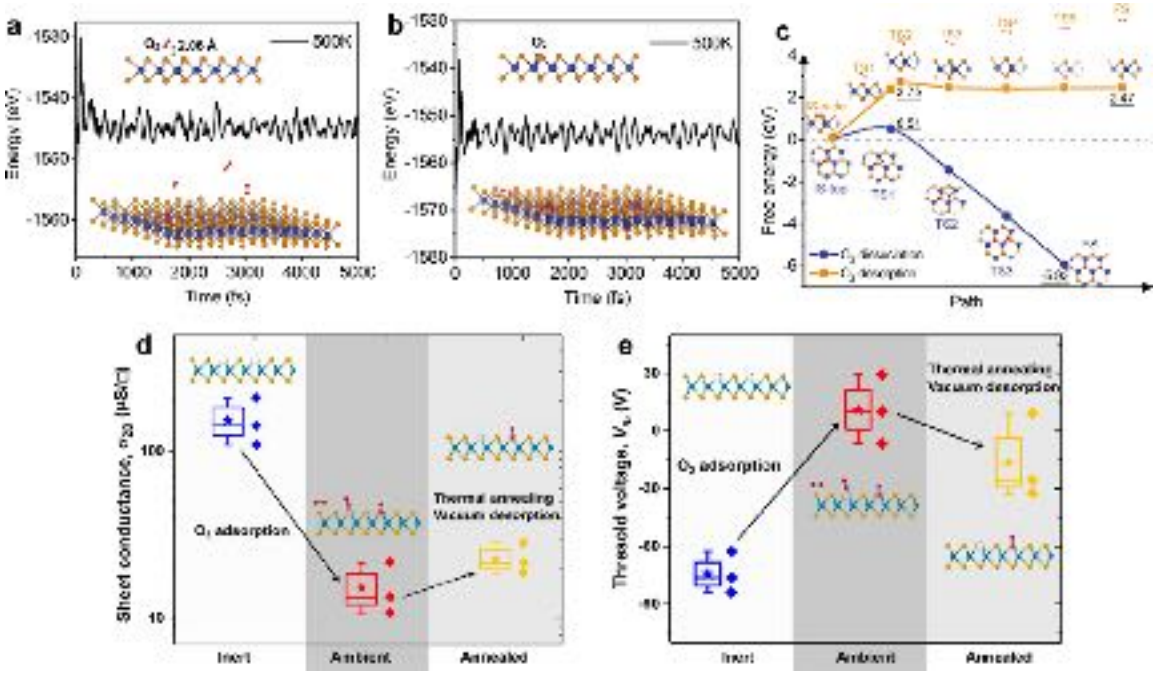

Figure 6. Reversibility of O_2 chemisorption. ***Ab initio*** **molecular dynamics (AIMD) simulation of (a) physisorbed and (b) chemisorbed O_2 at 500 K. The simulations indicate that ~75% of physisorbed O_2 molecules desorb at 500 K, while no chemisorbed O_2 molecules desorb. (c) Gibbs free energy profile of the initial state (IS), transition state (TS), and final state (FS) of O_2 dissociation and desorption on MoS_2 with adjacent double sulfur vacancies. The calculations show that desorption becomes energetically unfavorable once the O_2 molecules are chemisorbed. Instead, the dissociation of O_2 molecules is the more energy-favorable pathway. (d) Sheet conductance and (e) threshold voltages of inert and ambient MoS_2 devices. The devices were subsequently annealed at 473 K in a 10% H_2/Ar forming gas environment for 2 h. Annealing partially recovers the conductance attributed to the desorption of physisorbed O_2. However, chemisorbed O_2 molecules restrict its complete recovery.**

35.9 ± 1.8 $cm^2/(V\ s)$ (18.5 ± 1.4 $cm^2/(V\ s)$), and the mean sheet conductance increases by a factor of ~26 (10) to 23.6 ± 1.9 μS/□ (7.1 ± 0.8 μS/□).

We can understand the nature of the mobility improvement for inert devices from variable temperature electrical measurements (Supporting Information Figures S20 and S21). Figure 4c shows the temperature dependence of the carrier mobilities of mono- and bilayer MoS_2 devices from 300 to 80 K. At room (low) temperature, mobilities are typically phonon- (impurity-) scattering limited resulting in the observed $\mu \propto T^{-\gamma}$ trend.[57] Comparison of measurements at 80 and 300 K shows that the mobility increases by a factor of ~4 (3) to 470.8 ± 0.2 $cm^2/(V\ s)$ (106.3 ± 0.3 $cm^2/(V\ s)$) for exfoliated MoS_2 (WS_2) devices. We measure similarly high mobility improvement by a factor of ~3 (3) for monolayer CVD MoS_2 (WS_2) devices (Figure 4d). In contrast, the exfoliated ambient MoS_2 device shows only a modest 19% improvement, suggesting that higher impurity scattering from ambient exposure limits the low-temperature carrier mobility. To rule out poor contacts as the cause of the different mobility trends between ambient and inert devices, we verified that all analyzed devices exhibit linear output behavior at both room and low temperatures (Supporting Information Figures S18 and S20). Transfer length method measurements corroborate our device contact quality showing that both ambient and inert devices exhibit low contact resistances. Additionally, we find that minimizing ambient exposure can improve contact quality. Inert devices show lower contact resistance R_c = 10 ± 2 kΩμm compared to ambient devices where R_c = 15 ± 50 kΩμm (Supporting Information Figure S22). This lower R_c can be understood by the decreased *p*-doping of contact regions which decreases Schottky barrier heights.[58] The performance advantage of inert devices also extends to other key figures of merit, where we find consistent improvements in gate hysteresis and interface trap densities (Supporting Information Figure S24). Dual sweep transfer characteristics of inert and ambient MoS_2 (Figure S23a–b) and WS_2 (Figure S23c–d) FETs reveal a pronounced hysteresis window in all ambient devices. This clockwise hysteresis indicates charge trapping at the defect sites, likely associated with p-type defects, as evidenced by the reduced electron current during the reverse sweep compared to the forward sweep. We find a correlation between the hysteresis window and the interfacial trap density extracted from the subthreshold slope. The statistics are presented in Figure S24 for both MoS_2 and WS_2 FETs.

Next, we benchmarked our device performance with other devices of similar architecture as reported in the literature. We summarize sheet conductance and mobility values of exfoliated 2D MoS_2 (Figure 5a), CVD monolayer (Figure 5b) MoS_2, and WS_2 (Figure 5c) devices. Our exfoliated mono- and bilayer MoS_2 FETs demonstrate record room-temperature mobility of ~91 and ~132, respectively, more than three times higher than previous reports of comparable device geometries. Likewise, we measure a record high mobility of 36 $cm^2/(V\ s)$ for our WS_2 FET. The comparatively modest improvement for WS_2 is likely due to crystal quality limitations such that transport is still defect-limited, whereas MoS_2 growth processes are more mature. Notably, our MoS_2 mobility marks a significant advance toward the theoretical expectations for phonon-limited transport in monolayer 2D MoS_2 (indicated by the horizontal red dashed line in Figure 5a). The representative bilayer MoS_2 device exhibits the highest recorded mobility

https://doi.org/10.1021/acsnano.5c00995
ACS Nano 2025, 19, 9327−9339

value in comparable device architectures to date, regardless of the number of layers. We have found that minimizing ambient exposure to molecular oxygen leads to superior devices. We also benchmark mobility as a function of the channel thickness. We find that our inert device performance approaches the IRDS target and exceeds those of other state-of-the-art 2D FETs on high-k substrates, traditional ultrathin body (UTB) silicon PMOS and NMOS, and III−V MOSFETs at comparable channel thicknesses (Figure 5d), further highlighting the potential of 2D materials for ultrascaled electronics. Note that our fabrication strategy is generally compatible with most reported contact, dielectric, and interface engineering techniques, which can further improve device performance.

These measurements and benchmarking highlight the significant impact of O_2 adsorption at the device level. Next, we investigate the reversibility of adsorption processes. Based on our DFT calculated E_{ad} (Figure 1b), weakly interacting physisorption should be reversible through simple annealing or vacuum cycling treatments. However, the large E_{ad} of O_2 chemisorption poses a significant barrier toward molecular desorption and will require considerable thermal energies. While 2D TMDs can remain structurally intact up to 500 °C,[80] devices may not tolerate similarly high temperatures. In integrated circuit manufacturing, back-end-of-line (BEOL) compatibility is an essential consideration with a temperature limit of ∼400 °C.[5] Thermal effects such as strain and atomic diffusion at the contacts, dielectrics, and interfaces can degrade device performance and reliability at even lower temperatures below 300 °C.[21] With these considerations, we perform *ab initio* molecular dynamics (AIMD) simulation to understand the desorption process at elevated temperatures. We simulate O_2 molecules physisorbed and chemisorbed to TMD surfaces with double V_S (Figure 6a,b). At a temperature of 500 K, 75% (0%) of physisorbed (chemisorbed) O_2 molecules can desorb from the TMD surface. Importantly, our simulations (Figure 6c) suggest that chemisorbed O_2 molecules are more likely to undergo dissociative oxidation than desorb from the TMD surface. This is consistent with our previous work, where XPS measurements confirmed the tendency for dissociative oxidation in defective 2D WS_2 with double.[40] Our theoretical results therefore suggest the following scenario: inert devices exhibit the highest performance because the TMD surface is largely free of O_2 adsorbates. The TMD surface becomes increasingly saturated upon ambient exposure with a mixture of physisorbed and chemisorbed O_2. Prolonged exposure can even lead to dissociative oxidation, altering the TMD stoichiometry (as observed by XPS, Figure S1). While vacuum annealing can remove physisorbed O_2 and partially recover performance, chemisorbed O_2 remains on the surface, preventing full recovery. We expect a significant performance gap between inert and ambient devices even after thermal annealing.

To verify this, we experimentally assess the reversibility of device performance after thermal annealing under vacuum at 200 °C for 2 h. Figure 6d shows the box plots of sheet conductance measured for inert, ambient, and annealed devices. As expected, inert devices show the highest mean sheet conductance of 153.7 ± 29.3 μS/□ while ambient devices show the lowest mean sheet conductance of 15.2 ± 3.3 μS/□. Post thermal annealing under vacuum, the mean sheet conductance of ambient devices improves by ∼50% to 22.8 ± 2.9 μS/□ but remains far below that of inert devices. Similarly, the threshold voltage of the transistor can be partially restored through thermal annealing; however, complete recovery is unattainable as shown in Figure 6e.

CONCLUSION

We have identified the detrimental effect of oxygen on 2D TMD devices that were previously thought to be ambient stable. Adopting an oxygen-free fabrication approach, we push our device performance toward the theoretical phonon-limited intrinsic mobility. Our work highlights that atomically thin materials require radical strategies beyond conventional nanofabrication. This provides guidance for the community, which should adopt practices to limit oxygen exposure to 2D materials. Our study advances the understanding of 2D TMDs that can likely be expanded to other atomically thin vdW systems. Thousands of 2D materials have been theoretically predicted since the first isolation of graphene,[81] but experimental research has been largely restricted to a handful of 2D materials that are more ambient stable. Our oxygen-free fabrication approach should accelerate the fundamental understanding of 2D materials and their translation for practical applications.

METHODS

Materials. WS_2 and MoS_2 bulk crystals obtained from 6Carbon Technology and HQ Graphene were used for exfoliation. Commercial monolayers of MoS_2 and WS_2 grown by chemical vapor deposition (CVD) on sapphire substrates from 6Carbon Technology were employed for CVD-based devices. A 300 nm SiO_2-coated doped Si wafer served as the device substrate and gate dielectric in back-gated field-effect transistor (FET) device architectures.

Sample Preparation. The fabrication processes for both inert and ambient devices were carried out using the same equipment, including the spin-coater, hot plate, lithography tool, and metal evaporator to eliminate inconsistency in equipment and process conditions (details provided below). For inert devices, all fabrication steps including exfoliation, were performed inside a glovebox with O_2 and H_2O levels maintained typically below 5 ppm. In contrast, while the ambient devices were fabricated with the same tools, they were regularly exposed to ambient conditions in between steps to simulate the fabrication environment of a standard cleanroom. In particular, the exfoliation, development, and liftoff steps were performed entirely outside the glovebox.

Initially, fresh substrates were cleaned under N_2 purging, followed by baking at 100 °C for 10 min. Exfoliation of 2D layers was performed using low-adhesive blue tape. First, thicker layers were cleaved from parent crystals and exfoliated 5−6 times within the same tape to thin down the layers and cover the entire tape surface. Subsequently, the 2D layers were lightly pressed onto the cleaned substrates immediately after removal from the hot plate. Finally, the samples were inspected under an optical microscope to identify the desired thickness of 2D layers.

CVD-grown monolayers were transferred from sapphire to the SiO_2/Si substrate using a polymer-assisted wet-transfer method. The CVD TMD films were delaminated from their growth substrates under ambient conditions and transferred inside the inert glovebox after vacuum cycling in the antechamber. We conducted hot plate annealing before the final film transfer to the device substrate for fabrication. These combined annealing and vacuum treatments aim to eliminate physisorbed adsorbates.

Nanolithography. Contact patterning was conducted in an inert glovebox using a thermal scanning probe lithography (*t*-SPL) system (NanoFrazor Scholar, Heidelberg Instruments). A bilayer *t*-SPL resist consisting of 30/110 nm PPA/PMMA-MA was spin-coated, followed by baking at 140 °C for 90 s and 110 °C for 120 s, respectively. Details for the pattering parameters can be found in our previous study.[82] After thermal patterning, the exposed PMMA-MA layer was

https://doi.org/10.1021/acsnano.5c00995
ACS Nano 2025, 19, 9327−9339

etched in 20 °C ethanol for 15 s. Subsequently, the In/Au metals (5/35 nm) were deposited by thermal evaporation (0.1 Å/s) at ∼4 × 10^{-8} mbar with a substrate temperature of 0 °C. The same liftoff process was used for both inert and ambient devices but was performed inside and outside the glovebox, respectively. Liftoff was performed at room temperature for 10 min in Microposit 1165 solution.

To rule out the effect of the nanolithography method used in device fabrication on the observed improvement, we also define the exact width of metal contact by electron-beam lithography (EBL). Samples were spin-coated with PMMA A5 electron resist at 4000 rpm for 90 s, followed by hard baking at 180 °C for 2 min before removal from the glovebox. The resist-coated 2D layers were subsequently transferred to the EBL system. Next, the contacts were written by EBL, and In/Au metal (5/35 nm) was deposited via thermal evaporation. All the intermediate processes, such as sample development in MIBK/IPA (1:3), metal lift-off using 1165 solvent (Microposit), and further resist coating for the next step of lithography, were performed inside gloveboxes using interconnected sample-transfer lines without exposing the 2D materials to air at any stage.

Finally, the electrical connections and bond pads were defined by EBL, followed by 5/55 nm Cr/Au metal evaporation (0.1 Å/s). The same liftoff process was used for both inert and ambient devices but was performed inside and outside the glovebox, respectively. Liftoff was performed at 60 °C for 6 h in 1165 solution. Typical optical microscopic images of the exfoliated monolayers and the device after metal electrode fabrication are presented in Supporting Information (Figure S26).

Ambient Environment Fabrication. When possible, all process steps such as exfoliation, development, and liftoff, were explicitly performed in an ambient environment outside the glovebox.

Electrical Characterization. All devices were tested under similar conditions. Electrical measurements were carried out using a cryostat probe station under a base pressure of ∼1 × 10^{-4} mbar. The system was cooled down to 80 K using liquid nitrogen and the temperature was stabilized using a Lakeshore temperature controller. Measurements were conducted with Keithley 2450 source meter units, controlled by Python scripts.

X-ray Photoemission Spectroscopy. XPS measurements were carried out using an Al K_α source ($h\nu$ = 1486.7 eV) with a beam spot size of approximately 200 μm and an energy resolution of 0.3 eV. Photoelectrons were collected at a normal emission angle, while the incident light was aligned at 60° relative to the surface normal. Binding energies were calibrated against the Au 4f core level of a gold calibration standard sample. All XPS measurements were performed at room temperature.

Room-Temperature Optical Spectroscopy (Raman/PL). Room-temperature Raman and photoluminescence (PL) spectroscopy of monolayer MoS_2 and WS_2 were performed using an inVia Renishaw confocal Raman microscope. The point spectra were acquired with a 532 nm laser through a ×100 objective (NA = 0.85) and a 2400 lines/mm grating. To avoid unintentional laser-induced heating and sample degradation, the excitation power was kept below 50 μW. In-plane mapping was performed over a defined area scan using the same laser excitation for both the pristine and air-exposed sample. Since the optical measurements were conducted under ambient conditions, therefore both samples were capped with a PMMA (same use as an electron beam lithography resist) by spin-coating at 4000 rpm for 40 s. Pristine monolayers were exfoliated, and immediately spin-coated inside glovebox, while air-exposed samples were exfoliated outside, left in ambient for 4 h, and then spin-coated with PMMA layer under identical conditions to ensure consistency in sample preparation.

Low-Temperature Micro-PL Spectroscopy. For low-temperature photoluminescence (LT-PL), sample was mounted in a cryostat (Janis ST-500) and placed on a motorized stage. A 594 nm CW laser was used for excitation, where the linearly polarized beam was focused onto the sample using a ×50 Olympus objective (NA = 0.6). The emitted PL was collected via the same objective, converted back to linear polarization, and passed through a 600 nm long pass filter to block excitation light. The signal was dispersed by a spectrograph (Acton SP300) and detected using a EMCCD camera (Princeton Instruments).

Computational Details. A monolayer TMD was considered with a single chalcogen vacancy as a defect site, and the influence of different defect densities was investigated. The amount of charge modulation in TMDs due to molecular adsorption is ascribed by Δq. The orientation of O_2 molecules determines the actual E_{ad} and Δq values. For example, side-on O−O configurations exhibiting stronger adsorption (E_{ad} = 2.336 eV) and higher electron transfer (Δq = 1.080 e) compared to the end-on arrangements (E_{ad} = 1.98 eV and Δq = 1.031 e). The equilibrium band structure and atomic projected density of states (APDOS) are illustrated in ESI. Details about the DFT calculations and *ab initio* molecular dynamics (AIMD) simulations can be found in the Supporting Information.

ASSOCIATED CONTENT

Supporting Information

The Supporting Information is available free of charge at https://pubs.acs.org/doi/10.1021/acsnano.5c00995.

XPS data, computational details of DFT analysis, additional DFT results for pristine and defective MoS_2 and WS_2, cleanbox scheme, additional optical spectroscopy data, additional electrical data, DFT analysis on impact of O_2 exposure on effective mass, experimental results of O_2 exposure on contact resistance, optical images (PDF)

AUTHOR INFORMATION

Corresponding Authors

Yee Sin Ang − *Science, Mathematics and Technology, Singapore University of Technology and Design, Singapore 487372, Republic of Singapore;* orcid.org/0000-0002-1637-1610; Email: yeesin_ang@sutd.edu.sg

Kuan Eng Johnson Goh − *Quantum Innovation Centre (Q.InC), Agency for Science Technology and Research (A*STAR), Singapore 138634, Republic of Singapore; Institute of Materials Research and Engineering (IMRE), Agency for Science, Technology and Research (A*STAR), Singapore 138634, Republic of Singapore; Department of Physics, National University of Singapore, Singapore 117551, Republic of Singapore; Division of Physics and Applied Physics, School of Physical and Mathematical Sciences, Nanyang Technological University, Singapore 637371, Republic of Singapore;* orcid.org/0000-0003-0599-9696; Email: kejgoh@yahoo.com

Chit Siong Lau − *Quantum Innovation Centre (Q.InC), Agency for Science Technology and Research (A*STAR), Singapore 138634, Republic of Singapore; Institute of Materials Research and Engineering (IMRE), Agency for Science, Technology and Research (A*STAR), Singapore 138634, Republic of Singapore; Science, Mathematics and Technology, Singapore University of Technology and Design, Singapore 487372, Republic of Singapore;* orcid.org/0000-0002-6590-070X; Email: aaron_lau@imre.a-star.edu.sg

Authors

Subhrajit Mukherjee − *Quantum Innovation Centre (Q.InC), Agency for Science Technology and Research (A*STAR), Singapore 138634, Republic of Singapore; Institute of Materials Research and Engineering (IMRE), Agency for Science, Technology and Research (A*STAR), Singapore*

https://doi.org/10.1021/acsnano.5c00995
ACS Nano 2025, 19, 9327−9339

138634, Republic of Singapore; orcid.org/0000-0003-2674-1264
Shuhua Wang − *Science, Mathematics and Technology, Singapore University of Technology and Design, Singapore 487372, Republic of Singapore*
Dasari Venkatakrishnarao − *Institute of Materials Research and Engineering (IMRE), Agency for Science, Technology and Research (A*STAR), Singapore 138634, Republic of Singapore; Department of Chemistry, IIT Bombay, Mumbai 400076, India;* orcid.org/0000-0002-9019-2864
Yaoju Tarn − *Institute of Materials Research and Engineering (IMRE), Agency for Science, Technology and Research (A*STAR), Singapore 138634, Republic of Singapore*
Teymour Talha-Dean − *Institute of Materials Research and Engineering (IMRE), Agency for Science, Technology and Research (A*STAR), Singapore 138634, Republic of Singapore; Department of Physics and Astronomy, Queen Mary University of London, London E1 4NS, U.K.*
Rainer Lee − *Quantum Innovation Centre (Q.InC), Agency for Science Technology and Research (A*STAR), Singapore 138634, Republic of Singapore; Institute of Materials Research and Engineering (IMRE), Agency for Science, Technology and Research (A*STAR), Singapore 138634, Republic of Singapore*
Ivan A. Verzhbitskiy − *Quantum Innovation Centre (Q.InC), Agency for Science Technology and Research (A*STAR), Singapore 138634, Republic of Singapore; Institute of Materials Research and Engineering (IMRE), Agency for Science, Technology and Research (A*STAR), Singapore 138634, Republic of Singapore;* orcid.org/0000-0001-5945-8276
Ding Huang − *Quantum Innovation Centre (Q.InC), Agency for Science Technology and Research (A*STAR), Singapore 138634, Republic of Singapore; Institute of Materials Research and Engineering (IMRE), Agency for Science, Technology and Research (A*STAR), Singapore 138634, Republic of Singapore*
Abhishek Mishra − *Quantum Innovation Centre (Q.InC), Agency for Science Technology and Research (A*STAR), Singapore 138634, Republic of Singapore; Institute of Materials Research and Engineering (IMRE), Agency for Science, Technology and Research (A*STAR), Singapore 138634, Republic of Singapore;* orcid.org/0000-0002-1267-2440
John Wellington John − *Quantum Innovation Centre (Q.InC), Agency for Science Technology and Research (A*STAR), Singapore 138634, Republic of Singapore; Institute of Materials Research and Engineering (IMRE), Agency for Science, Technology and Research (A*STAR), Singapore 138634, Republic of Singapore*
Sarthak Das − *Quantum Innovation Centre (Q.InC), Agency for Science Technology and Research (A*STAR), Singapore 138634, Republic of Singapore; Institute of Materials Research and Engineering (IMRE), Agency for Science, Technology and Research (A*STAR), Singapore 138634, Republic of Singapore;* orcid.org/0000-0001-9526-9819
Fabio Bussolotti − *Quantum Innovation Centre (Q.InC), Agency for Science Technology and Research (A*STAR), Singapore 138634, Republic of Singapore; Institute of Materials Research and Engineering (IMRE), Agency for Science, Technology and Research (A*STAR), Singapore 138634, Republic of Singapore;* orcid.org/0000-0001-8725-4545
Thathsara Deshani Maddumapatabandi − *Quantum Innovation Centre (Q.InC), Agency for Science Technology and Research (A*STAR), Singapore 138634, Republic of Singapore; Institute of Materials Research and Engineering (IMRE), Agency for Science, Technology and Research (A*STAR), Singapore 138634, Republic of Singapore;* orcid.org/0000-0002-5768-2423
Yee Wen Teh − *Science, Mathematics and Technology, Singapore University of Technology and Design, Singapore 487372, Republic of Singapore*

Complete contact information is available at: https://pubs.acs.org/10.1021/acsnano.5c00995

Author Contributions

S.M. and C.S.L. designed the experiments and carried out the transport measurements and data analysis. S.W. and Y.S.A. performed DFT and AIMD simulations. S.M., D.V., T.T.D, R.L. and Y.W.T contributed to the device fabrication and measurements. Y.T., S.M. and C.S.L. contributed to coding. F.B. and T.M. performed XPS studies. I.A.V., D.H., A.M., J.W.J, SD and K.E.J.G contributed to result interpretation and discussion. K.E.J.G., Y.S.A. and C.S.L. supervised the experiments and calculations. C.S.L. conceived the study. C.S.L. and S.M. wrote the manuscript with input from all authors.

Notes

The authors declare no competing financial interest.

ACKNOWLEDGMENTS

We acknowledge the funding support from the Agency for Science, Technology and Research (A*STAR) (#21709, C230917006, and C230917007). C.S.L. acknowledges the support from A*STAR under its MTC IRG grant no. M23M6c0103 and MTC YIRG grant no. M21K3c0124. K.E.J.G. acknowledges support from a Singapore National Research Foundation Grant (CRP21-2018-0001). D.H. acknowledges funding support from A*STAR Project C222812022 and MTC YIRG M22K3c0105. Y.S.A. is supported by the Singapore Ministry of Education Academic Research Fund Tier 2 (Award no. MOE-T2EP50221-0019). Y.S.A. and S.W. are supported by the SUTD-ZJU IDEA Thematic Research Grant under the award number SUTD-ZJU (TR) 202203. This research is supported by A*STAR under Q.InC Strategic Research and Translational Thrust.

REFERENCES

(1) Moore, G. E. Cramming more components onto integrated circuits. *Proc. IEEE* **1998**, *86*, 82−85.
(2) Uchida, K.; et al. Experimental study on carrier transport mechanism in ultrathin-body SOI nand p-MOSFETs with SOI thickness less than 5 nm. In *Digest. International Electron Devices Meeting*; IEEE, 2002..
(3) Zhu, K.; et al. The development of integrated circuits based on two-dimensional materials. *Nat. Electron.* **2021**, *4*, 775−785.
(4) Kim, K. S.; et al. The future of two-dimensional semiconductors beyond Moore's law. *Nat. Nanotechnol.* **2024**, *19*, 895.
(5) Das, S.; et al. Transistors based on two-dimensional materials for future integrated circuits. *Nat. Electron.* **2021**, *4*, 786−799.
(6) Cao, W.; et al. The future transistors. *Nature* **2023**, *620*, 501−515.
(7) Liu, Y.; et al. Promises and prospects of two-dimensional transistors. *Nature* **2021**, *591*, 43−53.
(8) Jayachandran, D.; et al. Three-dimensional integration of two-dimensional field-effect transistors. *Nature* **2024**, *625*, 276−281.

(9) Wu, P.; Zhang, T.; Zhu, J.; Palacios, T.; Kong, J. 2D materials for logic device scaling. *Nat. Mater.* **2024**, *23*, 23−25.
(10) Wang, Y.; Sarkar, S.; Yan, H.; Chhowalla, M. Critical challenges in the development of electronics based on two-dimensional transition metal dichalcogenides. *Nat. Electron.* **2024**, *7*, 638−645.
(11) Sohier, T.; Campi, D.; Marzari, N.; Gibertini, M. Mobility of two-dimensional materials from first principles in an accurate and automated framework. *Phys. Rev. Mater.* **2018**, *2*, 1−21.
(12) Zhang, C.; Wang, R.; Mishra, H.; Liu, Y. Two-Dimensional Semiconductors with High Intrinsic Carrier Mobility at Room Temperature. *Phys. Rev. Lett.* **2023**, *130*, 87001.
(13) Zhang, C.; Liu, Y. Phonon-limited transport of two-dimensional semiconductors: Quadrupole scattering and free carrier screening. *Phys. Rev. B* **2022**, *106*, 1−9.
(14) Amontree, J.; et al. Reproducible graphene synthesis by oxygen-free chemical vapour deposition. *Nature* **2024**, *630*, 636−642.
(15) Zhang, T.; Wang, J.; Wu, P.; Lu, A.-Y.; Kong, J. Vapour-phase deposition of two-dimensional layered chalcogenides. *Nat. Rev. Mater.* **2023**, *8*, 799−821.
(16) Zhu, J.; et al. Low-thermal-budget synthesis of monolayer molybdenum disulfide for silicon back-end-of-line integration on a 200 mm platform. *Nat. Nanotechnol.* **2023**, *18*, 456−463.
(17) Wang, Y.; et al. Van der Waals contacts between three-dimensional metals and two-dimensional semiconductors. *Nature* **2019**, *568*, 70−74.
(18) Lau, C. S.; et al. Quantum Transport in Two-Dimensional WS_2 with High-Efficiency Carrier Injection through Indium Alloy Contacts. *ACS Nano* **2020**, *14*, 13700−13708.
(19) Shen, P.-C. C.; et al. Ultralow contact resistance between semimetal and monolayer semiconductors. *Nature* **2021**, *593*, 211−217.
(20) Wang, Y.; et al. P-type electrical contacts for 2D transition-metal dichalcogenides. *Nature* **2022**, *610*, 61−66.
(21) Li, W.; et al. Approaching the quantum limit in two-dimensional semiconductor contacts. *Nature* **2023**, *613*, 274−279.
(22) Su, T.; et al. Semimetal contacts to monolayer semiconductor: weak metalization as an effective mechanism to Schottky barrier lowering. *J. Phys. D Appl. Phys.* **2023**, *56*, 234001.
(23) Jiang, J.; et al. Yttrium-doping-induced metallization of molybdenum disulfide for ohmic contacts in two-dimensional transistors. *Nat. Electron.* **2024**, *7*, 545.
(24) Kiriya, D.; Tosun, M.; Zhao, P.; Kang, J. S.; Javey, A. Air-Stable Surface Charge Transfer Doping of MoS_2 by Benzyl Viologen. *J. Am. Chem. Soc.* **2014**, *136*, 7853−7856.
(25) Gao, H.; et al. Tuning Electrical Conductance of MoS_2 Monolayers through Substitutional Doping. *Nano Lett.* **2020**, *20*, 4095−4101.
(26) McClellan, C. J.; Yalon, E.; Smithe, K. K. H.; Suryavanshi, S. V.; Pop, E. High Current Density in Monolayer MoS_2 Doped by AlO_x. *ACS Nano* **2021**, *15*, 1587−1596.
(27) Choi, M. S.; et al. High carrier mobility in graphene doped using a monolayer of tungsten oxyselenide. *Nat. Electron.* **2021**, *4*, 731−739.
(28) Ma, N.; Jena, D. Charge scattering and mobility in atomically thin semiconductors. *Phys. Rev. X* **2014**, *4*, 1−9.
(29) Lau, C. S.; et al. Gate-Defined Quantum Confinement in CVD 2D WS_2. *Adv. Mater.* **2022**, *34*, 2103907.
(30) Zhang, Y.; et al. Liquid-Metal-Printed Ultrathin Oxides for Atomically Smooth 2D Material Heterostructures. *ACS Nano* **2023**, *17*, 7929−7939.
(31) Lau, C. S.; et al. Dielectrics for Two-Dimensional Transition-Metal Dichalcogenide Applications. *ACS Nano* **2023**, *17*, 9870−9905.
(32) Knobloch, T.; et al. Improving stability in two-dimensional transistors with amorphous gate oxides by Fermi-level tuning. *Nat. Electron.* **2022**, *5*, 356−366.
(33) Yang, S.; Jiang, C.; Wei, S. Gas sensing in 2D materials. *Appl. Phys. Rev.* **2017**, *4*, 21304.
(34) Liu, H.; Han, N.; Zhao, J. Atomistic insight into the oxidation of monolayer transition metal dichalcogenides: From structures to electronic properties. *RSC Adv.* **2015**, *5*, 17572−17581.
(35) Hu, Z.; et al. Two-dimensional transition metal dichalcogenides: Interface and defect engineering. *Chem. Soc. Rev.* **2018**, *47*, 3100−3128.
(36) Chhowalla, M.; et al. The chemistry of two-dimensional layered transition metal dichalcogenide nanosheets. *Nat. Chem.* **2013**, *5*, 263−275.
(37) Li, Q.; Zhou, Q.; Shi, L.; Chen, Q.; Wang, J. Recent advances in oxidation and degradation mechanisms of ultrathin 2D materials under ambient conditions and their passivation strategies. *J. Mater. Chem. A* **2019**, *7*, 4291−4312.
(38) Gao, J.; et al. Aging of Transition Metal Dichalcogenide Monolayers. *ACS Nano* **2016**, *10*, 2628−2635.
(39) Rao, R.; Islam, A. E.; Campbell, P. M.; Vogel, E. M.; Maruyama, B. In situ thermal oxidation kinetics in few layer MoS_2. *2D Mater.* **2017**, *4*, 025058.
(40) Bussolotti, F.; et al. Role of S-Vacancy Concentration in Air Oxidation of WS_2 Single Crystals. *ACS Nano* **2024**, *18*, 8706.
(41) Atkin, P.; et al. Laser exposure induced alteration of WS_2 monolayers in the presence of ambient moisture. *2D Mater.* **2018**, *5*, 015013.
(42) Kotsakidis, J. C.; et al. Oxidation of Monolayer WS_2 in Ambient Is a Photoinduced Process. *Nano Lett.* **2019**, *19*, 5205−5215.
(43) Wang, S.; Zhao, W.; Giustiniano, F.; Eda, G. Effect of oxygen and ozone on p-type doping of ultra-thin WSe_2 and $MoSe_2$ field effect transistors. *Phys. Chem. Chem. Phys.* **2016**, *18*, 4304−4309.
(44) Schmidt, H.; Giustiniano, F.; Eda, G. Electronic transport properties of transition metal dichalcogenide field-effect devices: surface and interface effects. *Chem. Soc. Rev.* **2015**, *44*, 7715−7736.
(45) Li, W. Electrical transport limited by electron-phonon coupling from Boltzmann transport equation: An ab initio study of Si, Al, and MoS_2. *Phys. Rev. B:Condens. Matter Mater. Phys.* **2015**, *92*, 1−10.
(46) Aryeetey, F.; Ignatova, T.; Aravamudhan, S. Quantification of defects engineered in single layer MoS_2. *RSC Adv.* **2020**, *10*, 22996−23001.
(47) Velický, M.; et al. Strain and Charge Doping Fingerprints of the Strong Interaction between Monolayer MoS_2 and gold. *J. Phys. Chem. Lett.* **2020**, *11*, 6112−6118.
(48) Melnikova-Kominkova, Z.; et al. Strong and efficient doping of monolayer MoS_2 by a graphene electrode. *Phys. Chem. Chem. Phys.* **2019**, *21*, 25700−25706.
(49) Sarkar, S.; et al. Anharmonicity in Raman-active phonon modes in atomically thin MoS_2. *Phys. Rev. B* **2020**, *101*, 205302.
(50) Chakraborty, B.; et al. Symmetry-dependent phonon renormalization in monolayer MoS_2 transistor. *Phys. Rev. B* **2012**, *85*, 161403.
(51) Chernikov, A.; et al. Electrical Tuning of Exciton Binding Energies in Monolayer WS_2. *Phys. Rev. Lett.* **2015**, *115*, 126802.
(52) Mak, K. F.; et al. Tightly bound trions in monolayer MoS_2. *Nat. Mater.* **2013**, *12*, 207−211.
(53) Plechinger, G.; et al. Trion fine structure and coupled spin−valley dynamics in monolayer tungsten disulfide. *Nat. Commun.* **2016**, *7*, 12715.
(54) Gray, M. J.; Kumar, N.; O'Connor, R.; Hoek, M.; Sheridan, E.; Doyle, M. C.; Romanelli, M. L.; Osterhoudt, G. B.; Wang, Y.; Plisson, V.; et al. A cleanroom in a glovebox. *Rev. Sci. Instrum.* **2020**, *91*, 073909.
(55) Fang, H.; et al. Degenerate n-Doping of Few-Layer Transition Metal Dichalcogenides by Potassium. *Nano Lett.* **2013**, *13*, 1991−1995.
(56) Smets, Q.; et al. Ultra-scaled MOCVD MoS_2 MOSFETs with 42nm contact pitch and 250μA/μm drain current. In *2019 IEEE International Electron Devices Meeting (IEDM)*; IEEE, 2019..
(57) Cui, X.; et al. Multi-terminal transport measurements of MoS_2 using a van der Waals heterostructure device platform. *Nat. Nanotechnol.* **2015**, *10*, 534−540.

https://doi.org/10.1021/acsnano.5c00995
ACS Nano 2025, 19, 9327−9339

(58) Jiang, J.; Xu, L.; Qiu, C.; Peng, L. M. Ballistic two-dimensional InSe transistors. *Nature* **2023**, *616*, 470−475.
(59) Liu, H.; Neal, A. T.; Ye, P. D. Channel length scaling of MoS_2 MOSFETs. *ACS Nano* **2012**, *6*, 8563−8569.
(60) Kappera, R.; et al. Phase-engineered low-resistance contacts for ultrathin MoS_2 transistors. *Nat. Mater.* **2014**, *13*, 1128−1134.
(61) Lockhart De La Rosa, C. J.; et al. Highly efficient and stable MoS_2 FETs with reversible n-doping using a dehydrated poly(vinyl-alcohol) coating. *Nanoscale* **2017**, *9*, 258−265.
(62) Abraham, M.; Mohney, S. E. Annealed Ag contacts to MoS_2 field-effect transistors. *J. Appl. Phys.* **2017**, *122*, 115306.
(63) Park, Y.; Baac, H. W.; Heo, J.; Yoo, G. Thermally activated trap charges responsible for hysteresis in multilayer MoS_2 field-effect transistors. *Appl. Phys. Lett.* **2016**, *108*, 083102.
(64) Wang, X.; Feng, H.; Wu, Y.; Jiao, L. Controlled synthesis of highly crystalline MoS_2 flakes by chemical vapor deposition. *J. Am. Chem. Soc.* **2013**, *135*, 5304−5307.
(65) Smithe, K. K. H.; Suryavanshi, S. V.; Muñoz Rojo, M.; Tedjarati, A. D.; Pop, E. Low Variability in Synthetic Monolayer MoS_2 Devices. *ACS Nano* **2017**, *11*, 8456−8463.
(66) Smithe, K. K. H.; English, C. D.; Suryavanshi, S. V.; Pop, E. Intrinsic electrical transport and performance projections of synthetic monolayer MoS_2 devices. *2D Mater.* **2016**, *4*, 011009.
(67) Xiao, J.; et al. Record-high saturation current in end-bond contacted monolayer MoS_2 transistors. *Nano Res.* **2022**, *15*, 475−481.
(68) English, C. D.; Shine, G.; Dorgan, V. E.; Saraswat, K. C.; Pop, E. Improved contacts to MoS_2 transistors by ultra-high vacuum metal deposition. *Nano Lett.* **2016**, *16*, 3824−3830.
(69) Rai, A.; et al. Air Stable Doping and Intrinsic Mobility Enhancement in Monolayer Molybdenum Disulfide by Amorphous Titanium Suboxide Encapsulation. *Nano Lett.* **2015**, *15*, 4329−4336.
(70) Kaushik, V.; et al. Charge Transport in 2D MoS_2, WS_2, and MoS_2-WS_2 Heterojunction-Based Field-Effect Transistors: Role of Ambipolarity. *J. Phys. Chem. C* **2020**, *124*, 23368−23379.
(71) Yun, S. J.; et al. Synthesis of centimeter-scale monolayer tungsten disulfide film on gold foils. *ACS Nano* **2015**, *9*, 5510−5519.
(72) Chen, J.; et al. Synthesis of Wafer-Scale Monolayer WS_2 Crystals toward the Application in Integrated Electronic Devices. *ACS Appl. Mater. Interfaces* **2019**, *11*, 19381−19387.
(73) Lan, C.; Li, C.; Yin, Y.; Liu, Y. Large-area synthesis of monolayer WS_2 and its ambient-sensitive photo-detecting performance. *Nanoscale* **2015**, *7*, 5974−5980.
(74) Aji, A. S.; Solís-Fernández, P.; Ji, H. G.; Fukuda, K.; Ago, H. High Mobility WS_2 Transistors Realized by Multilayer Graphene Electrodes and Application to High Responsivity Flexible Photodetectors. *Adv. Funct. Mater.* **2017**, *27*, 1703448.
(75) Yokoyama, M.; et al. Extremely-thin-body InGaAs-On-Insulator MOSFETs on Si fabricated by direct wafer bonding. In *2010 International Electron Devices Meeting*; IEEE, 2010; pp 46−49..
(76) Alian, A.; et al. Impact of the channel thickness on the performance of ultrathin InGaAs channel MOSFET devices. In *2013 IEEE International Electron Devices Meeting*; IEEE, 2013; pp 437−440..
(77) Sebastian, A.; Pendurthi, R.; Choudhury, T. H.; Redwing, J. M.; Das, S. Benchmarking monolayer MoS_2 and WS_2 field-effect transistors. *Nat. Commun.* **2021**, *12*, 1−12.
(78) Zou, X.; et al. Interface engineering for high-performance top-gated MoS_2 field-effect transistors. *Adv. Mater.* **2014**, *26*, 6255−6261.
(79) Schmidt, M.; et al. Mobility extraction in SOI MOSFETs with sub 1nm body thickness. *Solid. State. Electron.* **2009**, *53*, 1246−1251.
(80) Bandaru, N.; et al. Effect of Pressure and Temperature on Structural Stability of MoS_2. *J. Phys. Chem. C* **2014**, *118*, 3230−3235.
(81) Mounet, N.; et al. Two-dimensional materials from high-throughput computational exfoliation of experimentally known compounds. *Nat. Nanotechnol.* **2018**, *13*, 246−252.
(82) Talha-Dean, T.; et al. Nanoironing van der Waals Heterostructures toward Electrically Controlled Quantum Dots. *ACS Appl. Mater. Interfaces* **2024**, *16*, 31738−31746.

https://doi.org/10.1021/acsnano.5c00995
ACS Nano 2025, 19, 9327−9339